scientific reports

OPEN

High current density electroreduction of CO_2 into formate with tin oxide nanospheres

Thuy-Duong Nguyen-Phan[1,2]✉, Leiming Hu[3], Bret H. Howard[1], Wenqian Xu[4], Eli Stavitski[5], Denis Leshchev[5], August Rothenberger[1], Kenneth C. Neyerlin[3]✉ & Douglas R. Kauffman[1]✉

In this study, we demonstrate three-dimensional (3D) hollow nanosphere electrocatalysts for CO_2 conversion into formate with excellent H-Cell performance and industrially-relevant current density in a 25 cm^2 membrane electrode assembly electrolyzer device. Varying calcination temperature maximized formate production via optimizing the crystallinity and particle size of the constituent SnO_2 nanoparticles. The best performing SnO_2 nanosphere catalysts contained ~ 7.5 nm nanocrystals and produced 71–81% formate Faradaic efficiency (FE) between –0.9 V and –1.3 V vs. the reversible hydrogen electrode (RHE) at a maximum formate partial current density of 73 ± 2 mA cm_{geo}^{-2} at –1.3 V vs. RHE. The higher performance of nanosphere catalysts over SnO_2 nanoparticles and commercially-available catalyst could be ascribed to their initial structure providing higher electrochemical surface area and preventing extensive nanocrystal growth during CO_2 reduction. Our results are among the highest performance reported for SnO_2 electrocatalysts in aqueous H-cells. We observed an average 68 ± 8% FE over 35 h of operation with multiple on/off cycles. In situ Raman and time-dependent X-ray diffraction measurements identified metallic Sn as electrocatalytic active sites during long-term operation. Further evaluation in a 25 cm^2 electrolyzer cell demonstrated impressive performance with a sustained current density of 500 mA cm_{geo}^{-2} and an average 75 ± 6% formate FE over 24 h of operation. Our results provide additional design concepts for boosting the performance of formate-producing catalysts.

Electrochemical reduction of CO_2 (CO_2RR) powered by renewable energy is an appealing approach to produce carbon–neutral chemical feedstocks and fuels. Formic acid (HCOOH), often electrochemically produced as formate (HCOO⁻), is an attractive CO_2RR product due to its wide uses in agricultural, chemical and pharmaceutical industries[1–4]. Formic acid/formate has also been identified as an emerging fuel for fuel cells[5,6], a liquid hydrogen carrier with high volumetric capacity (53 g of H_2 per liter)[7,8], and for biomass upgrading applications[9]. Industrial formic acid production from fossil fuel precursors is extremely carbon intensive[2], but electrochemically converting CO_2 to formate, followed by down-stream electrodialysis purification into formic acid[10], could provide a carbon neutral or carbon negative route for producing this versatile chemical.

Sn-based materials are some of the most effective CO_2RR electrocatalysts for formic acid/formate production[11–18]. However, the performance of most Sn-based catalysts is still inadequate for practical applications because of low current densities (typically 10 ~ 25 mA cm_{geo}^{-2} in aqueous H-cells; Table S1), high overpotentials, and poor long-term stability[11–24]. Therefore, further catalyst design efforts and demonstration in full-cell electrolyzer devices are required to boost CO_2-to-formate conversion, improve efficiency, and validate high current density operation in realistic device architectures.

The CO_2RR has a rich structure sensitivity, and substantial efforts have been devoted to improving performance by controlling the catalyst morphology, dimension, size, composition, crystallographic orientation, surface

[1]National Energy Technology Laboratory, 626 Cochrans Mill Road, P.O. Box 10940, Pittsburgh, PA 15236-0940, USA. [2]NETL Support Contractor, 626 Cochrans Mill Road, P.O. Box 10940, Pittsburgh, PA 15236-0940, USA. [3]National Renewable Energy Laboratory, Golden, CO 80401, USA. [4]X-Ray Science Division, Advanced Photon Source, Argonne National Laboratory, Argonne, IL 60439, USA. [5]Photon Sciences Division, National Synchrotron Light Source II, Brookhaven National Laboratory, Upton, NY 11973, USA. ✉email: ThuyDuong.NguyenPhan@netl.doe.gov; Kenneth.Neyerlin@nrel.gov; Douglas.Kauffman@netl.doe.gov

structure or defects[11,25–28]. For example, incorporating a second metal such as Cu, Pd, or Ni into Sn can tune the CO_2RR selectivity of Sn to CO with 80–90% Faradaic efficiency (FE)[29–31], while In, Bi, and Pd can strongly improve both formic acid selectivity and current density at lower overpotential[32–35]. Controlling the nanoscale surface structure could also tune the proportion of low-coordinated corner, edge, and terrace sites in the catalysts, which strongly impact the adsorption and activation of CO_2, as well as the formation of key intermediates[19,36,37]. Three-dimensionality (3D) is another CO_2RR electrocatalyst design consideration, and reports have described CO_2RR catalyst morphologies assembled from nanoscale building blocks, including spheres, flowers, sheets, dendrites, porous foams, inverse opals, and others[12–18,30,35,38–43]. These 3D structures can offer larger surface area and a high density of electrocatalytic active sites that can improve current density[12–16,27,35,39,40,42]. From this perspective, a high-performance SnO_2 electrocatalysts can be designed by combining the concepts of 3D morphology, surface structure, and size control to improve current density and formate selectivity.

Here we demonstrate a template-based synthetic approach to create hollow nanosphere catalysts constructed from SnO_2 nanocrystal building blocks. The crystallinity and size of the constituent SnO_2 nanocrystals were controlled by varying the calcination temperature and exhibited strong impact to the catalysts' formate selectivity and partial current density. The best-in-class nanospheres produced 71–81% formate Faradaic efficiency (FE) in a broad potential range and achieved a maximum formate partial current density of 73 ± 2 mA cm_{geo}^{-2} at -1.3 V vs. RHE. The SnO_2 nanospheres also outperformed non-structured SnO_2 nanoparticles (nps) and commercially available SnO_2 nps catalysts. In situ Raman spectroscopy and time-dependent synchrotron-based X-ray diffraction (XRD) tracked the electrochemical reduction of SnO_2 nanospheres under steady-state CO_2RR conditions. The CO_2RR evaluation in a 25 cm² membrane electrode assembly (MEA) electrolyzer cell demonstrated sustained operation for 24 h at an industrially-relevant current density of 500 mA cm_{geo}^{-2}. Our results provide new design concepts for boosting the performance of formate-producing catalysts by controlling the surface structure to increase electrochemically-accessible surface area.

Methods

Synthesis of hierarchical hollow SnO_2 spheres.
All chemicals were purchased from Sigma-Aldrich and used as received without further purification. Hollow SnO_2 spheres were synthesized by a combined sol–gel and templating method. Spherical PMMA template particles with diameters of ~210 nm were prepared by surfactant-free emulsion polymerization using a cationic free radical initiator as described in the Supplementary Information. In a typical procedure, 226 mg of tin (II) chloride dihydrate ($SnCl_2.2H_2O$) were dissolved in 5 mL of ethanol (C_2H_5OH, 200 proof) and 38 mg of anhydrous citric acid ($C_6H_8O_7$) were separately mixed in 5 mL of ethanol. The citric solution was then added into the tin precursor and sonicated for 15 min. 1.5 mL of tin-citric solute ion was added dropwise into 30 mL of aqueous PMMA latex template (0.5 wt%) under vigorous stirring at room temperature. After 30 min of stirring, the mixture was evaporated overnight in the oven at 60 °C to obtain the as-synthesized powders. The same stock tin-citric solution was used to make multiple batches of as-synthesized materials which were subsequently annealed in static air at 300, 400, 500 and 600 °C for 3 h with ramping rate of 1 °C min^{-1}. The obtained powder was denoted as "SnO_2 nanospheres".

Non-templated SnO_2 nps were prepared using the same procedure, except the 30 ml of deionized water (DIW) did not contain the PMMA dispersion. After evaporation at 60 °C, the as-synthesized sample was subsequently calcined in air at 500 °C with a ramping rate of 1 °C min^{-1} for 3 h and named "non-templated SnO_2 nps". Commercial SnO_2 nanopowder with a heterogeneous particle size distribution between 5 and 150 nm (Sigma) was also used as reference material and denoted as "com-SnO_2 nps".

Electrochemical CO_2 reduction in an H-cell.
Electrochemical experiments were performed in a gas-tight, two-compartment H-cell separated by a Nafion 117 proton exchange membrane which was described in previous work[40]. Each compartment was filled with 60 mL of aqueous 0.1 M $KHCO_3$ electrolyte (99.99%, Sigma-Aldrich) and contained 90 mL headspace. Ultra-pure DIW with 18.3 MΩ cm^{-1} resistivity (Barnstead EASYpure LF) was used in all electrochemical experiments. The catholyte was continuously bubbled with CO_2 (99.999%, Butler gas) at a flow rate of 20 mL min^{-1} (pH ~ 6.8) under vigorous stirring during the experiments[40]. The counter and reference electrodes were Pt mesh and Ag/AgCl (saturated NaCl, BASi®), respectively. The catalyst ink was composed of 2.8 mg of the powder catalysts, 0.32 mg Vulcan VC-X72 carbon black, and 40 μL of Nafion® 117 solution binder (Sigma-Aldrich, 5%) in 400 μL of methanol. Working electrodes were fabricated by drop-casting the ink onto PTFE-coated carbon paper (Toray paper 060, Alfa Aesar) and N_2-dried. The mass loadings were kept at 9.5 ± 0.6 mg_{ink} cm_{geo}^{-2} (corresponding to 5.4 ± 0.3 mg_{SnO2} cm_{geo}^{-2}). All potentials were referenced against the reversible hydrogen electrode (RHE) (unless otherwise specified), and the uncompensated ohmic resistance was automatically corrected at 85% (iR-correction) using the instrument software in all electrochemical experiments[40].

CO_2 electroreduction tests were performed at room temperature using a SP-300 potentiostat (BioLogic Science Instrument). Short-term chronoamperometric experiments were conducted for 20 min at each applied potential between -0.6 V and -1.3 V vs. RHE and the products were collected every 20 min. Each data point is an average of at least three independent experiments on different fresh electrodes. Long-term chronoamperometric experiments were conducted over several days at -1.2 V vs. RHE and the testing was run for 5 h per day. After each day, the electrodes were discarded from the electrolyte, rinsed with DIW, and stored under ambient conditions in polystyrene petri dish. Fresh aqueous $KHCO_3$ catholyte was used for each cycle. The total and partial current densities were normalized to the exposed geometric area of the catalyst (unless otherwise specified).

The evolved gas products were collected in Tedlar gas-tight bags (Supelco) and then quantified by PerkinElmer Clarus 600 gas chromatography equipped with both FID and TCD detectors, using a ShinCarbon ST 80/100 Column and He carrier gas. The liquid products collected from the catholytes were filtered with a 0.22 μm PES

filter and determined by Dionex ICS-5000 + ion chromatography using ED50 conductometric detector, ASRS suppressor in auto-generation mode, AS11-HC column and gradient KOH eluent. The calculation of Faradaic efficiency (FE) for all products and formation selectivity is described in the Supplementary Information.

Electrochemical CO_2 reduction measurement in full MEA electrolyzer.　MEA full cell characterization was performed using custom-built hardware with an active area of 25 cm^2 previously reported in Chen et al.'s work[44]. The anode was a 25 cm^2 Ni foam (MFNi16m, MTI Corporation) with a thickness of 1.6 mm that was placed against a triple serpentine flow channel. Polytetrafluoroethylene (PTFE) gaskets with a thickness of 1.55 mm were used to achieve an anode electrode compression of 91%.

A commercial bipolar membrane (BPM) (FBM, Fumatech GmbH, Fuel Cell Store) was used with the cation exchange layer (crosslinked poly-ether ketone) facing the cathode, and the anion exchange layer (polysulfone with bicyclic amines) facing the anode. The catholyte flow channel had a thickness of 1.27 mm and was designed as a serpentine shape with four evenly spaced fingers, with each finger having a width of 2 mm. The cathode GDE was prepared by painting SnO_2 catalyst ink onto a gas diffusion layer (Sigracet 39BB GDL, Fuel Cell Store). Vulcan XC72R carbon powder was added to the ink to obtain a catalyst to carbon weight ratio of 1:1. A 5 wt% Nafion ionomer (D521 Nafion Dispersion, 1100 EW, Fuel Cell Store) was added to the ink with an ionomer to carbon weight ratio of 0.6:1. The fabricated GDE had a SnO_2 loading of 0.5 mg cm^{-2}. The cathode PTFE gasket was chosen to achieve a GDE compression of 18%.

The cell was heated to 60 °C during experiments and humidified CO_2 gas was supplied to the cathode at a relative humidity of 100% and a gas flow rate of 2 SLPM. The flow rates of 0.4 M K_2SO_4 catholyte and 1 M KOH anolyte were 40 ml min^{-1} and 50 ml min^{-1}, respectively. The liquid samples were filtered with a 0.22 μm PTFE syringe filter and then analyzed using Agilent 1260 Infinity II Bio-inert high-performance liquid chromatography. The gas products were collected with multi-layer foil gas sampling bags (Supel™, Sigma-Aldrich) and analyzed using Agilent 4900 Micro gas chromatography.

Materials characterizations.　Scanning electron microscopy (SEM) imaging was performed on a FEI Quanta 600F microscope operated at 10–20 kV equipped with an energy-dispersive X-ray (EDX) detector. High-resolution transmission electron microscopy (HR-TEM) was carried out on a FEI Titan Themis G2 200 Probe Cs Corrected Scanning Transmission Electron Microscope operated at accelerating voltage of 200 kV. The powder sample was suspended in ethanol, drop-casted onto a holey carbon-supported Cu grid, and naturally dried in air. TEM images of the post-reaction sample were prepared by scratching the electrode catalyst from carbon paper, sonicating with ethanol, and then dropping onto the TEM grid. X-ray powder diffraction (XRD) patterns were collected on a PANalytical X'Pert Pro X-ray diffractometer using CuKα radiation (λ = 1.5418 Å) at a scan rate of 0.2° min^{-1}.

Synchrotron X-ray diffraction measurements were conducted at beamline 17-BM-B (λ = 0.24121 Å) of the Advanced Photon Source at Argonne National Laboratory. Individual SnO_2 nanosphere electrodes were held at −1.2 V vs. RHE for fixed amounts of time in the H-cell (e.g. 0.5 h, 1 h, 5 h, 10 h, 20 h and 30 h). These post-reaction electrodes were then removed from the H-Cell after testing for a fixed amount of time, rinsed with DIW, immediately dried under flowing N_2, and wrapped with kapton tape to minimize air exposure. However, we do acknowledge that some reoxidation of the catalyst occurred between electrochemical testing and synchrotron XRD measurement. Two-dimensional diffraction patterns were collected by a Perkin Elmer amorphous silicon detector, data acquisition was performed with QXRD and the diffraction ring was integrated using GSAS-II freeware package[45].

Results and discussion

Materials characterizations.　The 3D SnO_2 hollow nanospheres were prepared by a combined sol–gel and templating approach (Fig. 1a). Negatively charged tin (II) citrate complex was absorbed on the surface of positively charged poly (methyl methacrylate) (PMMA) spheres (diameter of *ca.* 220 nm, Fig. S1) through electrostatic interaction. The system underwent hydrolysis, condensation, nucleation, and self-assembly to create tin-containing coating layers on the surface of the PMMA spheres. Subsequent calcination in air between 300 to 600 °C not only removed the PMMA template but also converted these coating layers into SnO_2 nanocrystals to produce hollow SnO_2 nanospheres (Fig. 1b and Figs. S2-S4).

A representative scanning electron microscope (SEM) image in Fig. 1b,c shows a SnO_2 nanosphere sample calcined at 500 °C having diameter of 205–210 nm. HR-TEM micrographs in Fig. 1d and Fig. S4 indicate the nanosphere walls were constructed from small, interconnected SnO_2 nanoparticles with sizes of 6–10 nm. The PMMA template fixed almost same diameter of nanospheres for all calcination temperatures, and XRD, EXAFS and XPS results (Fig. S5) further confirm tetragonal rutile structure (space group: $P4_2/mnm$, JCPDS 41–1445) and consistent Sn^{4+} oxidation state in all samples. Higher calcination temperatures produced sharper, more intense XRD peaks that indicate improved crystallinity and larger mean crystallite size. Figure 1e shows that the crystallite size increased from 2.5 nm to 10.5 nm when increasing the temperature from 300 °C to 600 °C. It is expected that the crystallinity and crystallite size of 3D SnO_2 nanospheres would impact the CO_2RR activity of SnO_2 nanospheres.

Electrochemical CO_2 reduction performance in conventional H-cell.　The CO_2RR performance of nanosphere catalysts was screened between −0.6 V and −1.3 V vs. RHE in a H-cell containing CO_2-saturated 0.1 M $KHCO_3$. Figure 2a shows representative FEs for formate, CO, and H_2 products vs. applied potentials for SnO_2 nanospheres calcined at 500 °C which were built from ~7.5 nm crystallite size. This nanosphere catalyst sample produced 71–81% formate FE between −0.9 V and −1.3 V vs. RHE, and the FE for C_1 products (formate
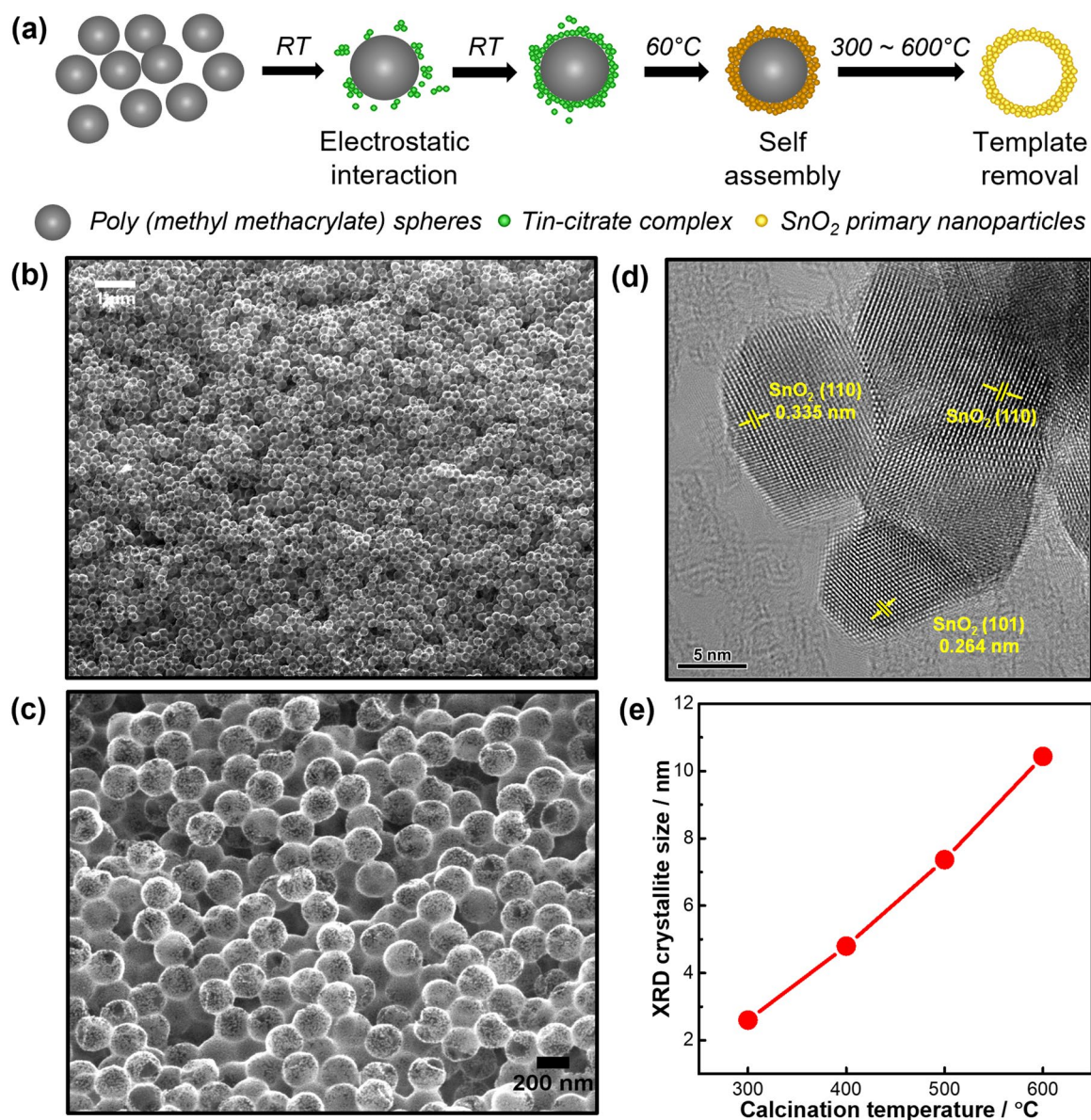
3

Figure 1. (**a**) Scheme illustrating the synthesis of 3D hollow SnO_2 nanospheres by a combined sol–gel and templating method. (**b,c**) Representative FE-SEM and (**d**) HR-TEM images of SnO_2 nanosphere calcined at 500 °C. (**e**) XRD crystallite size as function of calcination temperature.

and CO) reached > 90% between −0.8 V to −1.2 V vs. RHE (Fig. S6). SnO_2 nanospheres calcined at other temperatures also produced formate as a main product (Fig. S7), albeit with lower FEs than the 500 °C nanospheres, along with smaller amounts of CO and H_2. It is worth mentioning that gaseous CO and H_2 side-products (syngas) are easily separated from liquid formate for subsequent use in methanol or Fischer–Tropsch synthesis.

Figure 2b compares the formate partial current densities of SnO_2 nanospheres calcined at different temperatures, and 500 °C SnO_2 nanospheres produced the highest formate partial current density at all potentials (maximum value of 73 ± 2 mA cm_{geo}^{-2} at −1.3 V vs. RHE). This result implies an apparent dependency between CO_2RR performance and the size of the constituent SnO_2 nanocrystals. For example, SnO_2 nanospheres annealed at 300 °C contained the smallest SnO_2 nanocrystals (~ 3 nm) and produced the highest H_2 FE. This observation is also consistent with previous reports for increased H_2 production from small Sn, Cu, and Au nps and points to undercoordinated surface sites as likely H_2 evolution centers[19,29,52,53]. Higher calcination temperatures, *i.e.,* 400 and 500 °C, produced ~ 5 nm and ~ 7.5 nm SnO_2 nanocrystals, resulting in higher formate current densities and reduced H_2 production. Calcination at 600 °C further increased the nanocrystal diameter to > 10 nm and decreased formate production, which is qualitatively consistent with previous size-dependent results for SnO_2 catalysts[19]. Therefore, we suggest that SnO_2 nanospheres annealed at 500 °C likely produced an optimum balance between crystallinity and nanocrystal size, and thus maximized formate selectivity and partial current density. In fact, the data summarized in Fig. 2c and Table S1 demonstrate the 500 °C SnO_2 nanospheres produced some of the highest formate partial current densities ever reported for Sn, SnO_2 and SnO_2-carbon electrocatalysts in aqueous H-Cells[12,15,16,18,20–24,46–51].
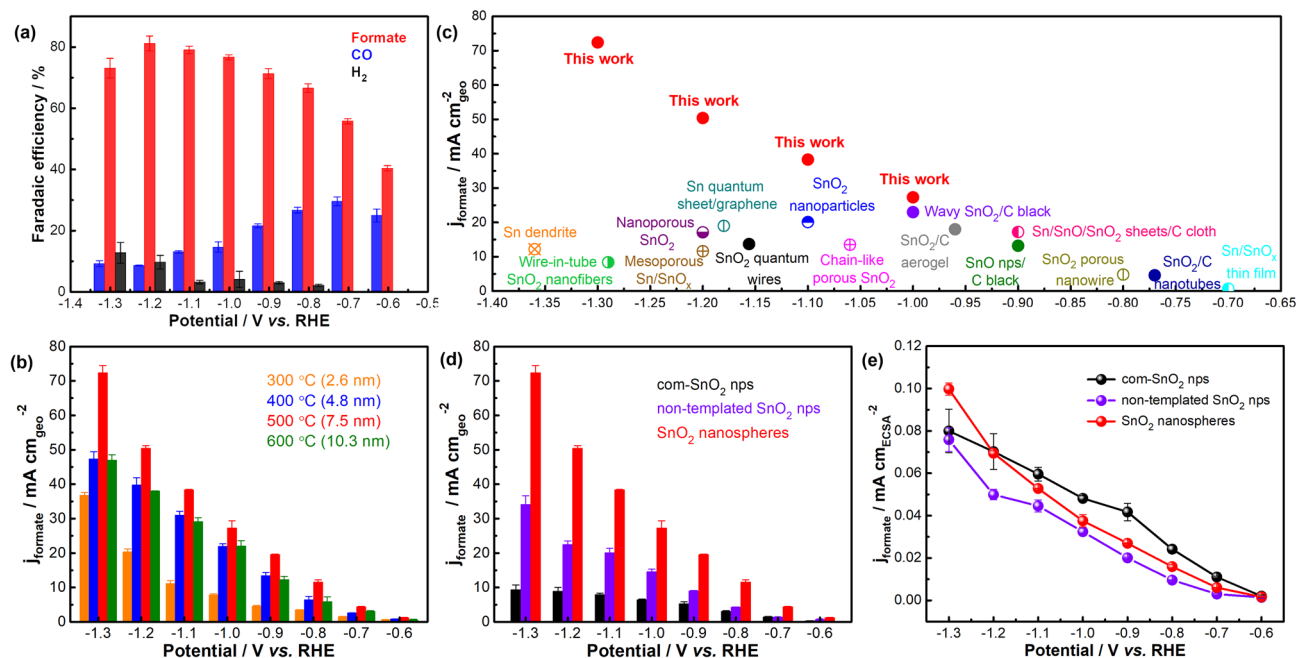
Figure 2. (**a**) Representative Faradaic efficiency for formate, CO, and H_2 vs. cathodic potentials for SnO_2 nanospheres calcined at 500 °C. (**b**) Potential-dependent formate partial current density as function of calcination temperature of SnO_2 nanospheres (aka SnO_2 crystallite size). (**c**) Comparison of CO_2RR performance for the best-performing SnO_2 nanospheres with previously reported Sn, SnO_2 and SnO_2-carbon electrocatalysts tested in a H-cell with bicarbonate electrolyte (mixed metal oxides, alloys, and doped systems are excluded): Sn dendrite[12], nanoporous SnO_2[15], SnO_2 porous nanowires[16], chainlike mesoporous SnO_2[18], Sn/SnO_x thin film[20], $Sn/SnO/SnO_2$ nanosheets/carbon cloth[21], wire-in-tube SnO_2 nanofibers[22], SnO_2 nanoparticles[23], ultrathin SnO_2 quantum wires[24], SnO_2/carbon nanotubes[46], Sn quantum sheet/graphene[47], SnO_2/carbon aerogel[48], SnO nanoparticles/carbon black[49], mesoporous Sn/SnO_x[50], wavy SnO_2/carbon black[51]. (**d,e**) Comparison of (**d**) geometric formate partial current density and (**e**) ECSA-normalized formate current density for commercially-available SnO_2 nps (com-SnO_2 nps), non-templated SnO_2 nps, and the best-performing SnO_2 nanospheres calcined at 500 °C.

We also compared the performance of non-templated, ~7 nm SnO_2 nps and commercially-available SnO_2 nanoparticles (named com-SnO_2 nps) with a heterogeneous size distribution between a few nanometers to hundreds of nanometers (Figs. S8 and S9). Figure 2d and Fig. S10 show a two ~ sixfold improvement in formate partial current density, 20–30% higher formate FE, and reduced H_2 evolution for the SnO_2 nanospheres compared with the non-templated and commercial SnO_2 nps. Impressively, total FE for the C_1 products for the 500 °C SnO_2 nanospheres was substantially higher than either non-templated or commercially available SnO_2 catalysts between −0.6 V and −1.3 V vs. RHE (Fig. S10).

We attribute the higher CO_2RR performance of SnO_2 nanospheres to a larger surface area, as confirmed with both BET and capacitance-based electrochemical surface area (ECSA) measurements[13,18,24,42] (Fig. S9, S11 and Table S2). In particular, the 500 °C nanospheres demonstrated 1.5–3 times larger ECSA than non-templated and commercially-available SnO_2 nanoparticles. These results confirm the nanosphere catalysts contained a higher density of electrocatalytic active sites to participate to CO_2RR. As shown in Fig. 2e, all three samples produced comparable ECSA-normalized formate partial current density, indicating that the total amount of electrochemically-active surface area was the dominant influence on *geometric* formate partial current density. In this regard, controlling the crystallinity and surface structure to maximize ECSA is a viable route for improving geometric current density.

The long-term electrolysis of SnO_2 nanospheres catalyst was conducted at −1.2 V vs. RHE in an H-cell over multiple start/stop cycles (Fig. 3a and Fig. S12). This potential produced the highest formate FE during short-term electrolysis experiments and on/off cycles mimicked operating with intermittent renewable electricity. The time-dependent formate partial current density is shown in Fig. 3a and the time-dependent FEs for formate, CO and H_2 are shown in Fig. S12. The catalyst showed a small initial decline in formate partial current density from ~ 55 mA cm_{geo}^{-2} in the first 5 h to an average 45 ± 5 mA cm_{geo}^{-2} over the next 30 h of operation, and we observed an average $68 \pm 8\%$ formate FE during the entire long-term experiment. Post-electrolysis electron microscopy in Fig. 3b–d revealed the SnO_2 nanocrystal size increased from ~ 7.5 nm to 15–25 nm. Conversely, as shown in Fig. 3a, non-templated SnO_2 nanoparticles produced much lower formate partial current density (~ 20 mA cm_{geo}^{-2}) and experienced severe particle agglomeration after 20 h (Fig. 3e). Similar particle size growth was also observed previously for other SnO_2 nanopowder electrocatalysts[18,39,54]. While the initial 3D nanosphere structure reconstructed during extended electrolysis, our results show the initial spherical structure prevented large-scale growth of the constituent SnO_2 nanocrystals, whereas non-templated SnO_2 nanoparticles experienced dramatic particle agglomeration.
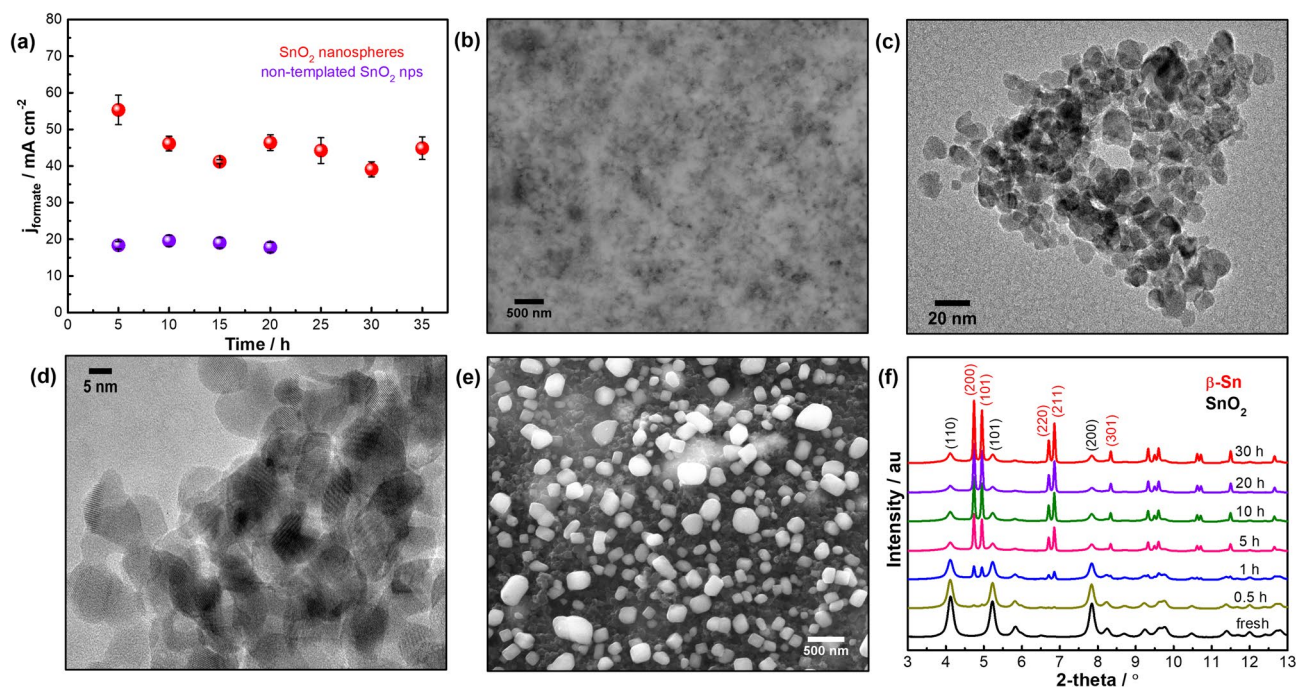
Figure 3. (**a**) Long-term CO_2RR performance of the best performing SnO_2 nanospheres and non-templated SnO_2 nps at −1.2 V vs. RHE. The experiments were run intermittently over multiple 5-h electrolysis periods. (**b**) Back-scattered SEM and (**c,d**) TEM images of SnO_2 nanospheres electrode after 35 h of operation. (**e**) SEM image of non-templated SnO_2 nps after 20-h electrolysis. (**f**) Time-dependent synchrotron-based XRD profiles of SnO_2 nanospheres collected at −1.2 V vs. RHE.

We conducted time-dependent, synchrotron-based XRD measurements to gain insight into the structural evolution of SnO_2 nanospheres during long-term electrolysis at −1.2 V vs. RHE. Figure 3f revealed the SnO_2 nanocrystals reduced into metallic Sn as evidenced by the emergence of body-centered tetragonal β-Sn diffraction peaks (space group: I4$_1$/*amd*). These results also indicate rapid transformation of SnO_2 into metallic Sn and an increase in crystallite size to *ca.* 23 nm under steady state operation (Fig. S13). Notably, this crystallite size remained stable over 30 h of operation and the XRD data agrees well with the post-electrolysis imaging in Fig. 3b–d that ruled out severe particle growth during long-term electrolysis. We also observed a minor residual oxide phase that likely resulted from reoxidation upon air exposure between electrochemical testing and XRD measurement.

Despite the literature containing multiple reports on in situ X-ray absorption, Raman and IR spectroscopies for SnO_2 CO_2RR catalysts[35,55–57], the results in Fig. 3f represent the first time-dependent XRD study to successfully track the phase change of SnO_2 catalysts as a function of CO_2RR electrolysis time. Despite some reoxidation between electrochemical testing and ex situ XRD measurements, our XRD results suggest the catalyst was reduced during CO_2RR at −1.2 V vs. RHE. This data strongly supports complementary in situ Raman spectroscopy experiments that showed the attenuation and then complete disappearance of SnO_2 characteristic bands at −1.2 V vs. RHE (Fig. S14). This result provides further evidence for the fast reduction of the SnO_2 surface to metallic Sn during CO_2RR and our observation is consistent with previous *operando* Raman results for other SnO_2 electrocatalysts[55,56]. Combined bulk and surface techniques in the present provide strong evidence that metallic Sn species are indeed the electrocatalytic active sites for converting CO_2 into formate.

CO_2 electroreduction to formate in high-performance membrane electrolyte assembly (MEA) electrolyzer.

Practical CO_2 conversion applications will require operating in electrolyzer devices at current densities of ∼ 100 s mA cm^{-2}[58]. Consequently, we evaluated the CO_2RR performance of SnO_2 nanosphere catalysts on 25 cm^2 gas diffusion electrodes (GDEs) in a recently reported MEA electrolyzer cell (details in the Methods Section)[44]. A thin aqueous catholyte layer between bipolar membrane (BPM) and cathode GDE reduced proton concentrations near the cathode interface, suppressed H_2 production, and transported away liquid products. This type of MEA full cell design can produce much higher current density than H-cells because gaseous CO_2 is delivered directly to the cathode, rather than converting CO_2 dissolved in aqueous electrolyte, and it allows catalyst evaluation under conditions that are more representative of scalable device architectures.

Figure 4a shows the initial polarization curve of the MEA cell operated at geometric current densities of 50–500 mA cm$_{geo}$$^{-2}$. The cell voltage and FE for formate increased with increasing current density and the cell reached current density of 500 mA cm$_{geo}$$^{-2}$ at 6.4 V with 86% formate FE (Fig. 4b). An equilibrium cell potential of 1.41 V is required for the CO_2 electrolysis to produce formic acid, however, due to the simultaneous formation of CO, the optimum voltage is above 3V[58]. As previously shown[44], approximately 43% of the cell voltage contribution stems from the BPM (junction and associated ion exchange layers), with 15% and 23% of the voltage
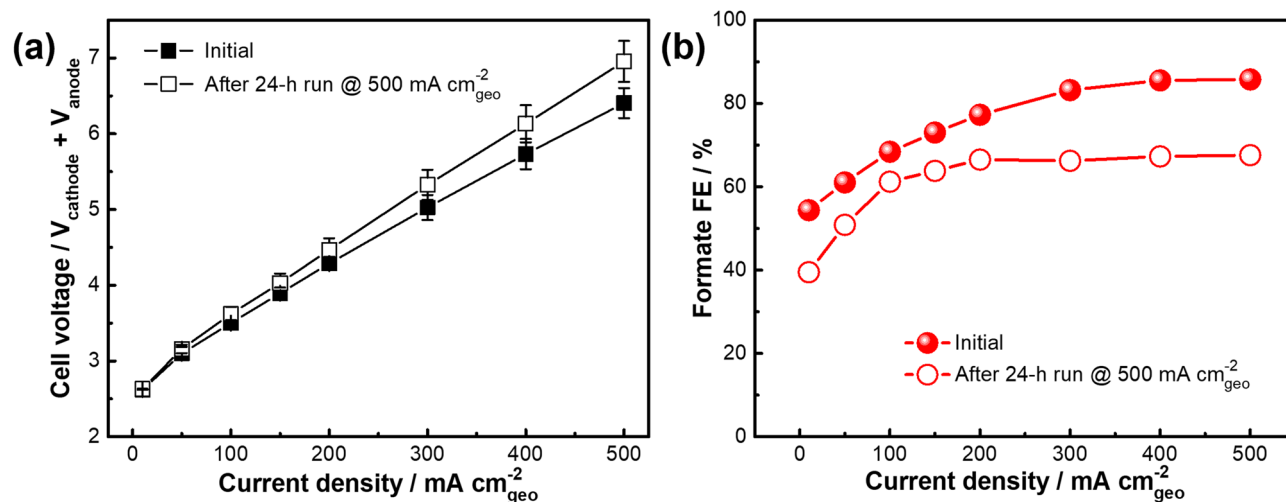
Figure 4. (**a**) MEA full cell polarization curves collected before and after a 24-h electrolysis at 500 mA cm_{geo}^{-2}. (**b**) Corresponding formate FEs vs. geometric current density. The MEA full cell contained a 5 cm × 5 cm cathode GDE decorated with SnO_2 nanospheres, a Ni foam anode, and a bipolar membrane with aqueous 0.4 M K_2SO_4 catholyte and aqueous 1 M KOH anolyte.

contribution coming from catholyte layer and the cathode overpotential, respectively. The cell was then held at a constant 500 mA cm^{-2} for 24 h and demonstrated an average 75 ± 6% formate FE (Fig. S15) and energy efficiencies between 14–19% (Fig. S16). We did observe a gradual increase in cell voltage over the 24-h test that was primarily associated with BPM degradation and oxidation of the Ni foam anode (Fig. S17). No nickel contamination from the anode was detected on the cathode GDE after the 24-h electrolysis (Fig. S18–S19). The BPM and anode were replaced, and the final polarization curve achieved 500 mA cm^{-2} current density and 68% formate FE (Fig. 4b), albeit at an approximately 9% higher cell voltage than the initial polarization. As summarized in Table S3, the sustained CO_2 conversion at 500 mA cm_{geo}^{-2} using a 25 cm^2 active electrode area in the present study is among the highest reported in the literature for pure SnO_2 catalysts in MEA electrolyzer cells[44,59,60]. The loss of formate FE over extended time run in an electrolyzer for Sn-based catalysts has been reported[58–60], however the opportunities still exist to further improve system performance through component-level optimization of the BPM[61], electrode and cell architecture, GDE transport property deterioration and flooding[62], and operational parameters.

Conclusions

We have reported SnO_2 nanosphere electrocatalysts constructed from small, interconnected SnO_2 nanocrystals for highly efficient CO_2 conversion into formate. Tuning thermal annealing temperatures maximized formate production by optimizing the crystallinity and particle size of the constituent SnO_2 nanoparticles. The best performing SnO_2 nanospheres demonstrated high Faradaic efficiencies, selectivities, and superior current densities toward formate production over a wide potential range in H-cell testing. SnO_2 nanospheres surpassed non-templated SnO_2 nps of similar size and commercially-available SnO_2 catalysts, which we attributed to larger electrochemical surface area. Finally, evaluation in a high-performance MEA full cell electrolyzer device demonstrated the SnO_2 nanospheres could sustain impressive CO_2 conversion into formate over 24-h at an industrially-relevant current density of 500 mA cm_{geo}^{-2}. Our work demonstrates the utility of incorporating 3D structure into CO_2RR electrocatalysts and provides additional catalyst design principles for improving performance.

Data availability

All data included in this study are available from the corresponding authors and can be provided upon request as needed.

References

1. Chen, X., Liu, Y. & Wu, J. Sustainable production of formic acid from biomass and carbon dioxide. *Mol. Catal.* **483**, 110716 (2020).
2. Olah, G. A., Goeppert, A. & Prakash, G. K. S. *Beyond Oil And Gas: The Methanol Economy, Third, Updated and Enlarged* (Wiley-VCH, 2018).
3. Hellstén, P. P., Salminen, J. M., Jørgensen, K. S. & Nystén, T. H. Use of potassium formate in road winter deicing can reduce groundwater deterioration. *Environ. Sci. Technol.* **39**, 5095–5100 (2005).
4. Lissner, H., Wehrer, M., Jartun, M. & Totsche, K. U. Degradation of deicing chemicals affects the natural redox system in airfield soils. *Environ. Sci. Pollut. Res.* **21**, 9036–9053 (2014).
5. Vo, T. *et al.* Formate: An energy storage and transport bridge between carbon dioxide and a formate fuel cell in a single device. *Chemsuschem* **8**, 3853–3858 (2015).

6. Ha, S., Larsen, R., Zhu, Y. & Masel, R. I. Direct formic acid fuel cells with 600 mA cm⁻² at 0.4 V and 22 °C. *Fuel Cells* **4,** 337–343 (2004).

7. Enthaler, S., von Langermann, J. & Schmidt, T. Carbon dioxide and formic acid-the couple for environmental-friendly hydrogen storage?. *Energy Environ. Sci.* **3**, 1207–1217 (2010).

8. Eppinger, J. & Huang, K.-W. Formic acid as a hydrogen energy carrier. *ACS Energy Lett.* **2**, 188–195 (2017).

9. Valentini, F. *et al.* Formic acid, a biomass-derived source of energy and hydrogen for biomass upgrading. *Energy Environ. Sci.* **12**, 2646–2664 (2019).

10. Ferrer, J. S. J., Laborie, S., Durand, G. & Rakib, M. Formic acid regeneration by electromembrane processes. *J. Membrane Sci.* **280**, 509–516 (2006).

11. Han, N., Ding, P., He, L., Li, Y. & Li, Y. Promises of main group metal–based nanostructured materials for CO₂ reduction to formate. *Adv. Energy Mater.* **10**, 1902338 (2020).

12. Won, D. H. *et al.* Rational design of a hierarchical tin dendrite electrode for efficient electrochemical reduction of CO₂. *Chemsuschem* **8**, 3092–3098 (2015).

13. Li, Y. N. *et al.* Rational design and synthesis of SnOₓ electrocatalysts with coralline structure for highly improved aqueous CO₂ reduction to formate. *ChemElectroChem* **3**, 1618–1628 (2016).

14. Fu, Y. *et al.* Novel hierarchical SnO₂ microsphere catalyst coated on gas diffusion electrode for enhancing energy efficiency of CO₂ reduction to formate fuel. *Appl. Energy* **175**, 536–544 (2016).

15. Liu, H. *et al.* Nanoporous tin oxides for efficient electrochemical CO₂ reduction to formate. *GreenChE.* **3**, 138–145 (2022).

16. Kumar, B. *et al.* Reduced SnO₂ porous nanowires with a high density of grain boundaries as catalysts for efficient electrochemical CO₂-into-HCOOH conversion. *Angew. Chem. Int. Ed.* **56**, 3644–3649 (2017).

17. Liang, C. *et al.* High efficiency electrochemical reduction of CO₂ beyond the two-electron transfer pathway on grain boundary rich ultra-small SnO₂ nanoparticles. *J. Mater. Chem. A* **6**, 10313–10319 (2018).

18. Bejtka, K. *et al.* Chainlike mesoporous SnO₂ as a well-performing catalyst for electrochemical CO₂ reduction. *ACS Appl. Energy Mater.* **2**, 3081–3091 (2019).

19. Zhang, S., Kang, P. & Meyer, T. J. Nanostructured tin catalysts for selective electrochemical reduction of carbon dioxide to formate. *J. Am. Chem. Soc.* **136**, 1734–1737 (2014).

20. Chen, Y. & Kanan, M. W. Tin oxide dependence of the CO₂ reduction efficiency on tin electrodes and enhanced activity for tin/tin oxide thin-film catalysts. *J. Am. Chem. Soc.* **134**, 1986–1989 (2012).

21. Wu, J. *et al.* Multivalent Sn species synergistically favours the CO₂-into-HCOOH conversion. *Nano Res.* **14**, 1053–1060 (2021).

22. Fan, L., Xia, Z., Xu, M., Lu, Y. & Li, Z. 1D SnO₂ with wire-in-tube architectures for highly selective electrochemical reduction of CO₂ to C₁ products. *Adv. Funct. Mater.* **28**, 1706289 (2018).

23. Daiyan, R. *et al.* Modulating activity through defect engineering of tin oxides for electrochemical CO₂ reduction. *Adv. Sci.* **6**, 1900678 (2019).

24. Liu, S. *et al.* Efficient electrochemical reduction of CO₂ to HCOOH over Sub-2 nm SnO₂ quantum wires with exposed grain boundaries. *Angew. Chem. Int. Ed.* **58**, 8499–8503 (2019).

25. Qiao, J., Liu, Y., Hong, F. & Zhang, J. A review of catalysts for the electroreduction of carbon dioxide to produce low-carbon fuels. *Chem. Soc. Rev.* **43**, 631–675 (2014).

26. Lu, Q., Rosen, J. & Jiao, F. Nanostructured metallic electrocatalysts for carbon dioxide reduction. *ChemCatChem* **7**, 38–47 (2015).

27. Vasileff, A., Zheng, Y. & Qiao, S. Z. Carbon solving carbon's problems: Recent progress of nanostructured carbon-based catalysts for the electrochemical reduction of CO₂. *Adv. Energy Mater.* **7**, 1700759 (2017).

28. Wang, Y., Han, P., Lv, X., Zhang, L. & Zheng, G. Defect and interface engineering for aqueous electrocatalytic CO₂ reduction. *Joule* **2**, 2551–2582 (2018).

29. Zhao, Y., Wang, C. & Wallace, G. G. Tin nanoparticles decorated copper oxide nanowires for selective electrochemical reduction of aqueous CO₂ to CO. *J. Mater. Chem. A* **4**, 10710–10718 (2016).

30. Zeng, J. *et al.* Advanced Cu-Sn foam for selectively converting CO₂ to CO in Aqueous solution. *Appl. Catal. B* **236**, 475–482 (2018).

31. Zhao, Y. *et al.* High crystallinity Sn crystals on Ni foam - Ideal bimetallic catalyst for electroreduction of CO₂ to syngas. *RSC Adv.* **10**, 39026–39032 (2020).

32. Lai, Q., Yang, N. & Yuan, G. Highly efficient In–Sn Alloy catalysts for electrochemical reduction of CO₂ to formate. *Electrochem. Commun.* **83**, 24–27 (2017).

33. Bai, X. *et al.* Exclusive formation of formic acid from CO₂ electroreduction by tunable Pd-Sn alloy. *Angew. Chem.* **129**, 12387–12391 (2017).

34. Xing, Y. *et al.* Bi@Sn core–shell structure with compressive strain boosts CO₂ electroreduction into formic acid. *Adv. Sci.* **7**, 1902989 (2020).

35. Wu, Z. *et al.* Engineering bismuth–tin interface in bimetallic aerogel with 3D porous structure for CO₂ reduction to HCOOH. *Angew. Chem. Int. Ed.* **60**, 12554–12559 (2021).

36. Gao, D. *et al.* Size-dependent electrocatalytic reduction of CO₂ over Pd nanoparticles. *J. Am. Chem. Soc.* **137**, 4288–4291 (2015).

37. Reske, R., Mistry, H., Behafarid, F., Cuenya, B. R. & Strasser, P. Particle size effects in the catalytic electroreduction of CO₂ on Cu nanoparticles. *J. Am. Chem. Soc.* **136**, 6978–6986 (2014).

38. Xie, J.-F. *et al.* Efficient electrochemical CO₂ reduction on a unique chrysanthemum-like Cu nanoflower electrode and direct observation of carbon deposite. *Electrochim. Acta* **139**, 137–144 (2014).

39. Zhang, X. X. *et al.* Intentional construction of high-performance SnO₂ catalysts with a 3D porous structure for electrochemical reduction of CO₂. *Nanoscale* **11**, 18715–18722 (2019).

40. Nguyen-Phan, T.-D. *et al.* Understanding three-dimensionally interconnected porous oxide-derived copper electrocatalyst for selective carbon dioxide reduction. *J. Mater. Chem. A* **7**, 27576–27584 (2019).

41. Wei, F. *et al.* Controllably engineering mesoporous surface and dimensionality of SnO₂ toward high-performance CO₂ electroreduction. *Adv. Funct. Mater.* **30**, 2002092 (2020).

42. Luo, W., Xie, W., Li, M., Zhang, J. & Züttel, A. 3D hierarchical porous indium catalyst for highly efficient electroreduction of CO₂. *J. Mater. Chem. A* **7**, 4505–4515 (2019).

43. Luo, W., Zhang, J., Li, M. & Züttel, A. Boosting CO production in electrocatalytic CO₂ reduction on highly porous Zn catalysts. *ACS Catal.* **9**, 3783–3791 (2019).

44. Chen, Y. *et al.* A robust, scalable platform for the electrochemical conversion of CO₂ to formate: Identifying pathways to higher energy efficiencies. *ACS Energy Lett.* **5**, 1825–1833 (2020).

45. Toby, B. H. & Von Dreele, R. B. GSAS-II: The genesis of a modern open-source all-purpose crystallography software package. *J. Appl. Cryst.* **46**, 544 (2013).

46. Pavithra, K. & Kumar, S. M. S. Embedding oxygen vacancies at SnO₂-CNT surfaces via a microwave polyol strategy towards effective electrocatalytic reduction of carbon-dioxide to formate. *Catal. Sci. Technol.* **10**, 1311–1322 (2020).

47. Lei, F. *et al.* Metallic tin quantum sheets confined in graphene toward high-efficiency carbon dioxide electroreduction. *Nat. Commun.* **7**, 12697 (2016).

48. Yu, J., Liu, H., Song, S., Wang, Y. & Tsiakaras, P. Electrochemical reduction of carbon dioxide at nanostructured SnO₂/carbon aerogels: The Effect of tin oxide content on the catalytic activity and formate selectivity. *Appl. Catal. A Gen.* **545**, 159 (2017).

49. Gu, J., Heroguel, F., Luterbacher, J. & Hu, X. Densely packed, ultra small SnO nanoparticles for enhanced activity and selectivity in electrochemical CO₂ reduction. *Angew. Chem. Int. Ed.* **57**, 2943 (2018).

50. Lai, Q., Yuan, W. Y., Huang, W. J. & Yuan, G. Q. Sn/SnOₓ electrode catalyst with mesoporous structure for efficient electroreduction of CO₂ to formate. *Appl. Surf. Sci.* **508**, 145221 (2020).

51. Chen, Z. *et al.* Wavy SnO₂ catalyzed simultaneous reinforcement of carbon dioxide adsorption and activation towards electrochemical conversion of CO₂ to HCOOH. *Appl. Catal. B Environ.* **261**, 118243 (2020).

52. Zhu, W. *et al.* Monodisperse Au nanoparticles for selective electrocatalytic reduction of CO₂ to CO. *J. Am. Chem. Soc.* **135**, 16833–16836 (2013).

53. Back, S., Yeom, M. S. & Jung, Y. Active sites of Au and Ag nanoparticle catalysts for CO₂ electroreduction to CO. *ACS Catal.* **5**, 5089–5096 (2015).

54. Xiang, H. *et al.* Production of formate by CO₂ electrochemical reduction and its application in energy storage sustain. *Energy Fuels* **4**, 277–284 (2020).

55. Dutta, A. *et al.* Probing the chemical state of tin oxide NP catalysts during CO₂ electroreduction: A complementary *operando* approach. *Nano Energy* **53**, 828–840 (2018).

56. Dutta, A., Kuzume, A., Rahaman, M., Vesztergom, S. & Broekmann, P. Monitoring the chemical state of catalysts for CO₂ electroreduction: An in operando study. *ACS Catal.* **5**, 7498–7502 (2015).

57. Baruch, M. F., Pander, J. E., White, J. L. & Bocarsly, A. B. Mechanistic insights into the reduction of CO₂ on tin electrodes using in situ ATR-IR spectroscopy. *ACS Catal.* **5**, 3148–3156 (2015).

58. Masel, R. I. *et al.* An industrial perspective on catalysts for low-temperature CO₂ electrolysis. *Nat. Nanotechnol.* **16**, 118–128 (2021).

59. Yang, H., Kaczur, J. J., Sajjad, S. D. & Masel, R. I. Electrochemical conversion of CO₂ to formic acid utilizing Sustainion™ membranes. *J. CO₂ Util.* **20**, 208–217 (2017).

60. Yang, H., Kaczur, J. J., Sajjad, S. D. & Masel, R. I. Performance and long-term stability of CO₂ conversion to formic acid using a three-compartment electrolyzer design. *J. CO₂ Util.* **42**, 101349 (2020).

61. Oener, S. Z., Foster, M. J. & Boettcher, S. W. Accelerating water dissociation in bipolar membranes and for electrocatalysis. *Science* **369**, 1099–1103 (2020).

62. Yang, K., Kas, R., Smith, W. A. & Burdyny, T. Role of the carbon-based gas diffusion layer on flooding in a gas diffusion electrode cell for electrochemical CO₂ reduction. *ACS Energy Lett.* **6**, 33–40 (2021).

Acknowledgements

Disclaimer

This project was funded by the United States Department of Energy, National Energy Technology Laboratory, in part, through a site support contract. Neither the United States Government nor any agency thereof, nor any of their employees, nor the support contractor, nor any of their employees, makes any warranty, express or implied, or assumes any legal liability or responsibility for the accuracy, completeness, or usefulness of any information, apparatus, product, or process disclosed, or represents that its use would not infringe privately owned rights. Reference herein to any specific commercial product, process, or service by trade name, trademark, manufacturer, or otherwise does not necessarily constitute or imply its endorsement, recommendation, or favoring by the United States Government or any agency thereof. The views and opinions of authors expressed herein do not necessarily state or reflect those of the United States Government or any agency thereof.

Author Contributions

The manuscript was written through contributions of all authors. T.-D.N.-P. developed the concepts and methodology, designed and performed all experimental work of catalyst synthesis, lab-based characterizations and H-cell testings, analyzed and interpreted all experimental data, and drafted the manuscript. L.H. and K.C.N. contributed to the methodology, validation and data acquisition of MEA electrolyzer testing, and manuscript drafting. B.H.H. conducted lab XRD measurement and data analysis. W.X. collected synchrotron XRD data. E.S. and D.L. contributed to XAS data collection. A.R. supported materials synthesis and lab-based characterization. D.R.K. developed the concepts, designed experiments, supervised and oversaw work, contributed to data analysis and interpretation, and drafted the manuscript. All authors contributed to the review and editing of the manuscript.

Competing interests

The authors declare no competing interests.

Additional information

Supplementary Information The online version contains supplementary material available at https://doi.org/10.1038/s41598-022-11890-6.

Correspondence and requests for materials should be addressed to T.-D.N.-P., K.C.N. or D.R.K.